

Experimental and 3D simulation study of a nitrogen–hydrogen fueled PEMFC

Jianfeng Zhao*, Qianchao Liang, Yifan Liang, Jinyi Hu

College of Power Engineering, Naval University of Engineering, Wuhan, P. R. China.
Correspondence: Jianfeng Zhao, College of Power Engineering, Naval University of Engineering,
Wuhan, 4 30033, P. R. China

*E-mail: jianfeng62300_zhao@163.com

Received: 26 November 2021 / *Accepted:* 4 January 2022 / *Published:* 2 February 2022

Ammonia, as a chemical storage carrier for hydrogen, exhibits high hydrogen storage density and easy storage advantages. However, the reconversion of ammonia to pure hydrogen requires additional energy consumption as well as complex equipment, thus greatly reducing its advantages as a hydrogen storage carrier. The development of a proton exchange membrane fuel cell (PEMFC) that directly uses ammonia decomposition gas as fuel, can avoid the purification of hydrogen and simplify the on-site hydrogen production system. Thus, the application of fuel cells can be greatly expanded. In this paper, the output characteristics of a PEMFC fueled by a nitrogen–hydrogen mixture equivalent to ammonia decomposition gas are first investigated experimentally. Then, a 3D simulation model of a PEMFC fueled by ammonia reforming gas is established based on the experimental data. The distribution of the local current density and local hydrogen concentration inside the fuel cell and the relationship between them are studied and analyzed. The optimal efficiency and fuel utilization of the fuel cell at different flow rates are investigated. Finally, a preliminary simulation analysis of the effect of anode length on the maximum output power of the fuel cell is conducted. The results of this study can provide a reference for the fuel control strategy of an ammonia reforming gas-fueled PEMFC and its optimization.

Keywords: ammonia reforming gas, PEMFC, local current density, optimization, fuel utilization

1. INTRODUCTION

As the global climate crisis due to the greenhouse effect continues to worsen, an increasing number of countries are focusing on the development of low-carbon or even zero-carbon emission economies. As of June 2021, 136 countries have committed to achieving a carbon neutrality target by the middle of the 21st century [1]. Low-carbon fuel technology is the main way to achieve a low-carbon economy; thus, the development of low-carbon or zero-carbon renewable fuel technology is a

hot spot of current research.

Research on low-carbon renewable fuel has mainly focused on the regeneration of light hydrocarbon fuels, such as methane, methanol, and ethanol, based on carbon dioxide and hydrogen; however, there are challenges in these energy cycles, such as carbon dioxide capture and carbon deposition [2-5].

Research on zero-carbon renewable fuels has mainly focused on physical hydrogen storage [6] or chemical hydrogen storage [7] based on the hydrogen cycle. Regarding physical hydrogen storage, in all current technologies, such as high-pressure hydrogen storage, cryogenic liquid hydrogen storage, and cryogenic critical hydrogen storage, hydrogen undergoes thermodynamic transformations, which can significantly increase the total storage and transportation costs [8]. Although hydrogen can also be stored in carbon nanotubes, metal hydrides, and hydrogen storage alloys under milder conditions, the weight density is limited [9,10]. Regarding chemical hydrogen storage, ammonia is a promising substance because it is liquid at a relatively low pressure of 10 bar, has a high energy density of 15.6 MJ L^{-1} compared to liquid hydrogen, which has an energy density of 9.1 MJ L^{-1} at cryogenic temperature or 5.6 MJ L^{-1} at high pressure of 70 MPa [11]. Moreover, ammonia has a high hydrogen concentration of 75 mol%, so it has high hydrogen storage density and easy storage advantages. Regarding the ammonia cycle, the gases involved are nitrogen and hydrogen, and since nitrogen is the main gas in the atmosphere, it can be easily obtained and rereleased back into the atmosphere during ammonia consumption; thus, the whole system is completely carbon-free. Ammonia is usually synthesized by the Haber-Bosch process, and green ammonia synthesis methods, such as electrochemical synthesis at low temperature and low pressure, have recently been investigated [12].

Fuel cells are capable of efficiently converting hydrogen into electricity, so fuel cell systems that use ammonia as the hydrogen storage medium are a hot research topic. Although ammonia can directly replace hydrogen as fuel for solid oxide fuel cells (SOFCs), in the case of proton exchange membrane fuel cells (PEMFCs), ammonia is a toxic gas, thereby needing to be converted to hydrogen; therefore, a more complex fuel conversion system is required. Since PEMFCs have been commercially applied in recent years [13], the study of PEMFCs with ammonia as the hydrogen storage medium has become increasingly studied. There are two important steps in the conversion of ammonia to hydrogen: one is the catalytic decomposition of ammonia, and the other is the purification of hydrogen. Research on the catalytic decomposition of ammonia has focused on microfluidic reactors [14] and the study of economical and efficient catalysts. The replacement of conventional ruthenium-based catalysts with iron–nickel alloys is being investigated by a Danish company (RenCat) and is expected to be successfully commercialized [15]. After the decomposition of ammonia, a mixture of nitrogen and hydrogen (crude hydrogen) is obtained, so further separation is required to obtain pure hydrogen. Separation methods for crude hydrogen include deep cooling separation, variable pressure adsorption, and membrane separation [16-18]. However, all of these methods suffer from the problem of oversized units, thus, achieving small and portable PEMFC on-site hydrogen production units has remained a goal. Therefore, the development of PEMFCs directly using ammonia decomposition gas is very meaningful and can greatly expand the application of PEMFCs.

Hunter et al. established an ammonia decomposition gas-PEMFC demonstration platform to demonstrate the feasibility of a PEMFC directly using ammonia decomposition gas [19]. There have

been many studies on the effect of nitrogen on PEMFCs, but the studies have mainly targeted the effect of trace amounts of nitrogen. Previous studies have shown that the long-term accumulation of nitrogen has an effect on the diffusion and transport of hydrogen within the fuel cell, but when pure hydrogen is used as the fuel, its final accumulation is not high and is periodically discharged along with the anode purge. Therefore, for a PEMFC using pure hydrogen as fuel, the main purpose of optimizing the flow channel geometry is to achieve optimal water management, thermal management and material distribution inside the cell [20-22]. However, for ammonia decomposition gas, experiments show that a high concentration of nitrogen significantly affects the operating state of the fuel cell. Moreover, with the consumption of hydrogen, the nitrogen concentration in the fuel cell increases along the fuel flow direction. Therefore, it is necessary to study and analyze the operating characteristics of fuel cells with high concentrations of nitrogen.

This paper first experimentally investigates the output characteristics of a PEMFC fueled by a nitrogen–hydrogen mixture (1:3 molar ratio of nitrogen to hydrogen) that is equivalent to ammonia decomposition gas, and then a three-dimensional simulation model of a PEMFC fueled with ammonia decomposition gas is established based on the experimental data. The distribution of the local current density and local hydrogen concentration inside the fuel cell and the relationship between them are studied and analyzed. The optimal efficiency and fuel utilization of the fuel cell at different flow rates are investigated. Finally, a preliminary simulation analysis of the effect of anode runner length on the maximum output power of the fuel cell is conducted. The results of the study can provide a reference for the fuel control strategy of an ammonia reforming gas-fueled PEMFC and its optimization.

2. MATERIALS AND METHODS

First, the experimental method of an ammonia decomposition gas-fueled PEMFC system is described. Then, the three-dimensional modeling method of the PEMFC using ammonia decomposition gas as a fuel is described. The main difference from the modeling method of a PEMFC using pure hydrogen as fuel is the species diffusion model inside the anode. When pure hydrogen is used as the fuel, hydrogen is the dominant gas in the anode with a concentration as high as 99.999%, which is an order of magnitude difference compared to the concentration of other impurity gases; thus, its species diffusion model is generally that for the transport of diluted species [23]. In contrast, when ammonia decomposition gas is used as fuel, the nitrogen concentration in the anode is on the same order of magnitude as that of hydrogen; thus, its species diffusion model is generally that for the transport of concentrated species [24].

2.1 Experimental system and method

The composition of the experimental system is shown in Figure 1. The main components of the system include a hydrogen gas source, a nitrogen–hydrogen mixture gas source, a fuel flow controller, a commercial PEMFC stack (51 cells, each with an effective area of 65 cm²) and a 2 kW electronic

load. During the experiments, the output characteristics of the PEMFC fueled by pure hydrogen are first tested at a flow rate of 9 L/min, and then the output characteristics of the PEMFC fueled by a nitrogen–hydrogen mixture are tested at a flow rate of 12 L/min (to ensure the same hydrogen equivalent flow rate).

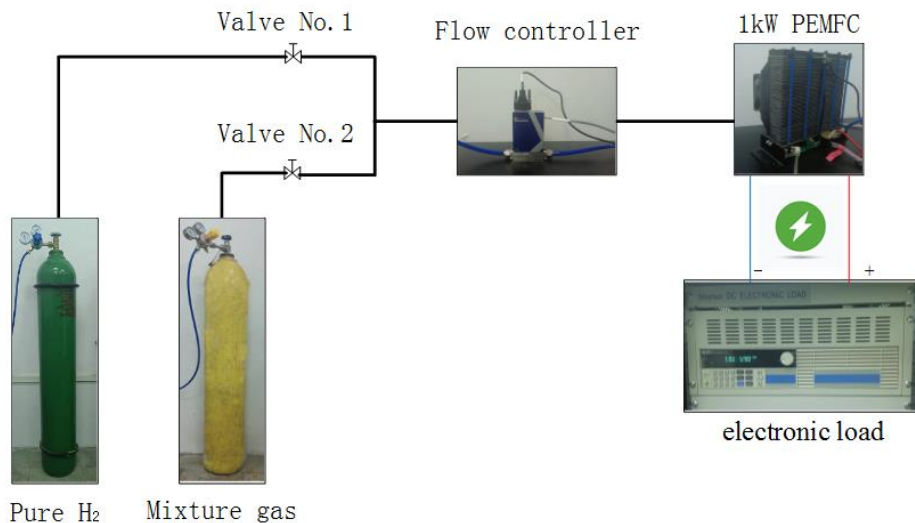


Figure 1. Schematic diagram showing the composition of the experimental system

Nomenclature	
i Current (SI unit: A)	μ Gas viscosity (SI unit: Pa s)
δ conductivity (SI unit: S m ⁻¹)	u Velocity (SI unit: m s ⁻¹)
Φ Potential (SI unit: V)	k Permeability (SI unit: m ²)
Q Current source(SI unit: A m ⁻¹)	ϵ Porosity
$\Phi_{s,c}$ Electronic potential in the upper surface of c_gdl (SI unit: V)	w_i Mass fraction of species i
$\Phi_{s,a}$ Electronic potential in the lower surface of a_gdl (SI unit: V)	R_i Chemical reaction rate of species i (SI unit: kg m ⁻³ s ⁻¹ or mol m ⁻³ •s ⁻¹)
E_{eq} Equilibrium potential (SI unit: V)	x_k Mole fraction of species k
η Overpotential (SI unit: V)	M_i Molecular mass of species i
F Faraday’s constant (SI unit: C mol ⁻¹)	D_i^m Equivalent diffusion coefficient of species i in a multicomponent mixture(SI unit: m ² /s)
$c_{i,ref}$ Material reference concentration (SI unit: mol m ⁻³),	τ Tortuosity factor.
$i_{0,a}$ and $i_{0,c}$ Standard exchange current density of the anode and cathode (SI unit: A m ⁻²)	c_i Concentration of species i (SI unit: mol/m ³)
R Gas constant	D_i Diffusion coefficient (SI unit: m ² /s)
T Temperature of the fuel cell (SI unit: K)	I Unit matrix
$\alpha_{a,a}, \alpha_{a,c}, \alpha_{c,a}, \alpha_{c,c}$ Transfer coefficients	P Pressure (SI unit: Pa)
ρ Density (SI unit: kg m ⁻³)	v_i Molar diffusion volume of gas (SI unit: cm ³ mol ⁻¹).
Subscripts	
i Gas components, Hydrogen H_2 , nitrogen N_2 , oxygen O_2 , water vapor H_2O	s electronic
l ion	e Anode a or cathode c
gdl a_gdl and c_gdl domains	cl a_cl and c_cl domains

2.2 Mathematical modeling

The PEMFC tested in the experiment is an air-cooled fuel cell (Figure 2(a)). The anode and cathode channels of the PEMFC are perpendicular to each other, and the flow directions of the air and fuel result in a crossflow. Theoretically, the air composition on the cathode side corresponding to different anode runners will change along the air flow direction (Figure 2(b)). However, since this PEMFC uses the cathode air for cooling, it leads to a much higher air mass flow rate at the cathode than the air mass required for the electrochemical reaction. The minimum air mass flow rate of the PEMFC cathode in the experiment is 77 times the required stoichiometric air mass at the rated power; thus, it can be estimated that the oxygen concentration at the cathode outlet is only 1.3% lower than that at the inlet. Therefore, to simplify the model, the gas composition in the cathode flow channel is assumed to be the same as that of air. Thus far, the modeling region of the model in this paper is shown in Figure 2(c), and the model is divided into seven regions by function: the anode flow channel (a_channel), anode diffusion layer (a_gdl), anode reaction layer (a_cl), proton exchange membrane (PEM), cathode reaction layer (c_cl), cathode diffusion layer (c_gdl), and cathode flow channel (c_channel). Additionally, referring to the literature [25-29], the following further assumptions are made.

- (1) The gases involved in the model are considered ideal gases.
- (2) The water generated at the cathode can evaporate rapidly and be removed with the cooling air; therefore, there is no accumulation of liquid water on the cathode side.
- (3) The operating temperature of the fuel cell is a constant value.
- (4) The reverse osmosis of water and nitrogen from the cathode side to the anode side is not considered in the model.

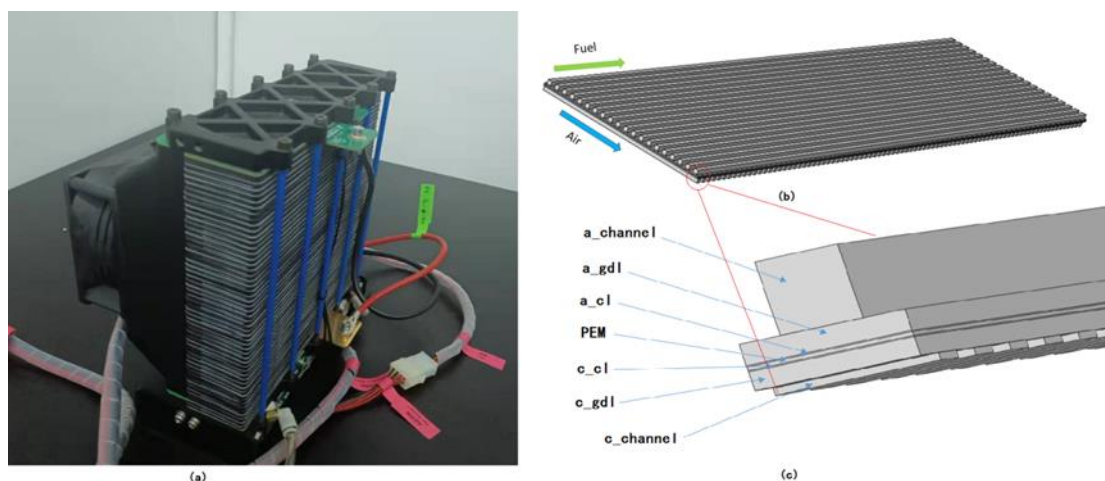


Figure 2. (a) Air-cooled PEMFC, (b) schematic showing the geometry of a single fuel cell, and (c) three-dimensional section of the model

2.2.1 Electric field model

The area of the electric field model contains the anode diffusion layer, the anode reaction layer,

the proton exchange membrane, the cathode reaction layer and the cathode diffusion layer. Among these, the anode and cathode reaction layers involve the electrochemical reaction model and the electric field model, while the anode diffusion layer, the cathode diffusion layer and the proton exchange membrane involve only the electric field model.

Electric field global control equation:

$$\begin{cases} \nabla \cdot i_l = Q_l, & i_l = -\delta_l \nabla \phi_l \\ \nabla \cdot i_s = Q_s, & i_s = -\delta_s \nabla \phi_s \end{cases} \quad (1)$$

The current source Q is zero in the anode diffusion layer, the cathode diffusion layer, and the proton exchange membrane. The ion current is zero in the anode and cathode diffusion layers, and the electron current is zero in the proton exchange membrane.

Fuel cell output voltage:

$$V = \phi_{s,c} - \phi_{s,a} \quad (2)$$

Here, $\phi_{s,a}$ is equal to 0.

The electrochemical potential E can be calculated from the Nernst equation[23]:

$$E = 1.229 - 0.85 \times 10^{-3} * (T - 298.15) + 4.3085 \times 10^{-5} * T * [\ln(P_{H_2}) + 0.5 * \ln(P_{O_2})] \quad (3)$$

Potential balance equation:

$$\eta = \phi_s - \phi_l - E_{eq} \quad (4)$$

where E_{eq} is set as 0 in the anode reaction layer and E in the cathode reaction layer. Furthermore, η is obtained from the local current density equation (Butler-Volmer equation).

Local current density i_a (Butler-Volmer equation):

$$i_{l,e} = i_{0,e} * C_e * \left(\exp\left(\frac{\alpha_{e,a} F \eta_e}{RT}\right) - \exp\left(\frac{-\alpha_{e,c} F \eta_e}{RT}\right) \right) \quad (5)$$

$$C_a = \left(\frac{c_{H_2}}{c_{H_2,ref}} \right)^{0.5} \quad (6)$$

$$C_c = \frac{c_{O_2}}{c_{O_2,ref}} \quad (7)$$

2.2.2 Flow field model

The area of the flow field model is the anode flow channel and the anode diffusion layer. The Navier–Stokes equation and Brinkman equation are adopted to describe the flow in the free zone (anode channel) and porous zone, respectively. The combination of the Navier–Stokes equation and continuity equation can be expressed as [30]:

$$(\rho u \cdot \nabla) u = -\nabla P + \nabla \cdot [\mu(\nabla u + (\nabla u)^T)] - \frac{2}{3} \mu(\nabla \cdot u) I \quad (8)$$

$$\nabla(\rho u) = 0 \quad (9)$$

The combination of the Brinkman equation and continuity equation can be expressed as [30]:

$$\frac{\mu}{k} u = -\nabla P + \nabla \cdot \left[\frac{1}{\varepsilon} [\mu(\nabla u + (\nabla u)^T)] - \frac{2}{3} \mu(\nabla \cdot u) I \right] \quad (10)$$

2.2.3 Gas diffusion model

The gas diffusion model is divided into two submodels, namely, the anode gas diffusion model and the cathode gas diffusion model. Each submodel contains the corresponding flow channel, diffusion layer and reaction layer regions. When the fuel is ammonia decomposition gas, the model takes into account two species at the anode (H_2 and N_2) and three species at the cathode (O_2 , H_2O and N_2). The diffusion of these mixtures can be described by the transport of concentrated species equations [30]:

$$\nabla j_i + \rho(u \cdot \nabla)w_i = R_i \quad (11)$$

where j_i is the diffusion mass flow density of species i , which is defined as follows:

$$j_i = -(\rho D_i^m \nabla w_i + \rho w_i D_i^m \frac{\nabla M_n}{M_n} - j_{c,i}) \quad (12)$$

$$D_i^m = \frac{1 - w_i}{\sum_{k \neq i} \frac{x_k}{D_{ik}}} \quad (13)$$

$$M_n = \left(\sum_i \frac{w_i}{M_i} \right)^{-1} \quad (14)$$

$$j_{c,i} = \rho w_i \sum_i \frac{M_i}{M_n} D_k^m \nabla x_k \quad (15)$$

where D_{ik} is the binary diffusion coefficient, which can be calculated by Fuller's empirical formula [31]:

$$D_{ik} = 3.198 * 10^{-8} * \frac{T^{1.75}}{P \left(v_i^{\frac{1}{3}} + v_k^{\frac{1}{3}} \right)^2} \left(\frac{1}{M_i} + \frac{1}{M_k} \right)^{0.5} \quad (16)$$

The binary diffusion coefficient obtained by Equation (20) needs to be modified in the porous region:

$$D_{ik,e} = \frac{\varepsilon}{\tau} D_{ik} \quad (17)$$

When high purity hydrogen is used as fuel, only H_2 and H_2O are present in the gas at the anode, and the H_2O content is very low. The multicomponent diffusion model is governed by the dilute matter transfer control equation [30].

$$\nabla \cdot (-D_i \nabla c_i) + u \cdot \nabla c_i = R_i \quad (18)$$

3. RESULTS AND DISCUSSION

3.1 Experimental results

Figure 3 shows the output characteristics of PEMFCs when hydrogen and a nitrogen–hydrogen mixture is used as fuel. The difference between the two cases is small when the current is less than approximately 20 A; however, as the current continues to increase, the output characteristics of pure hydrogen become increasingly better than those of the mixture. The maximum power of pure hydrogen

obtained in the experiment is 824 W, and the maximum power of the mixture is 759 W. Thus, is the mixture exhibits an 8% decrease in maximum power. Theoretically, the polarization loss of the fuel cell plays a dominant role in the initial phase of the voltammetric curve, with ohmic polarization in the middle part and concentration difference polarization at the end. Therefore, it can be seen from the voltammetric curves of the two that the difference between them is mainly due to the concentration polarization, which means that the presence of nitrogen increases the concentration polarization and decreases the output performance of the PEMFC.

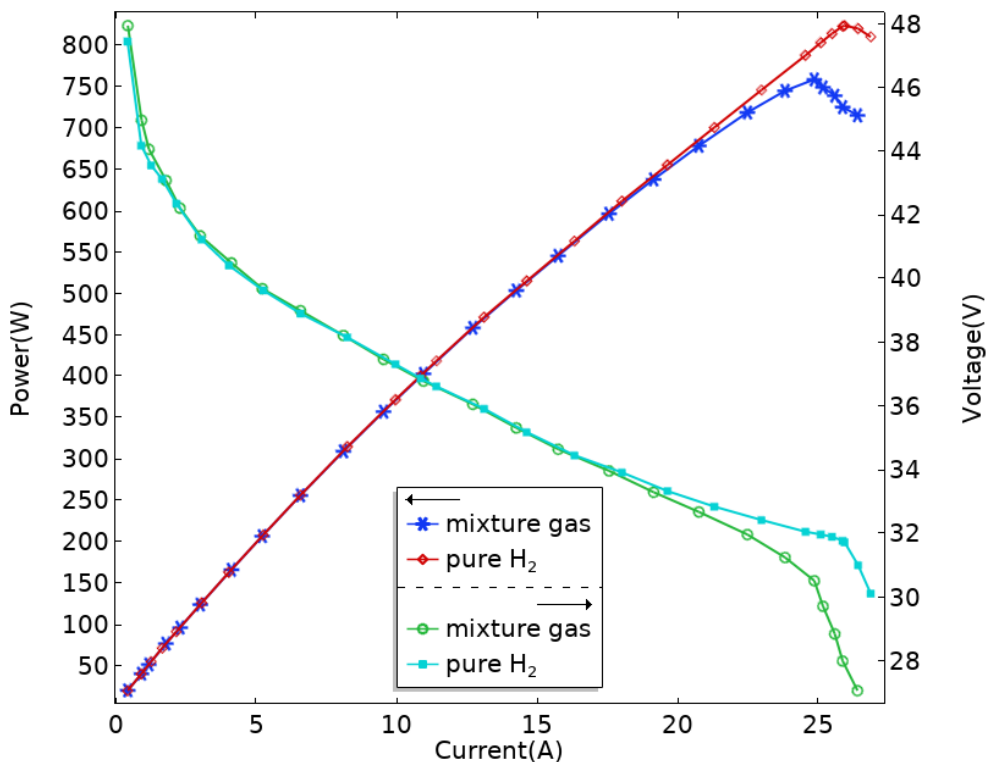


Figure 3. Experimental results

3.2. Verification of the simulation model

Table 1. Basic parameters of the fuel cell

Geometric parameters		
Parameters	Value	Ref.
Anode channel length, L (mm)	173	Measured data
Anode channel height, H (mm)	1	Measured data
Anode channel width, W_{an} (mm)	1	Measured data
Width of the rib, W_{rib} (mm)	1	Measured data
Anode channel width, W_{ca} (mm)	1	Measured data
Anode gas diffusion layer thickness, σ_{ad} (mm)	0.29	[26]
Cathode gas diffusion layer thickness, σ_{cd} (mm)	0.254	[26]

Anode catalyst layer thickness, σ_{ac} (mm)		0.0165	[26]	
Cathode catalyst layer thickness, σ_{cc} (mm)		0.0165	[26]	
PEM thickness, σ_m (mm)		0.0508	[26]	
Physical parameters of the fuel cell				
	Value	Ref.	Value	Ref.
σ_s	220	[32]	i_{0a}	1.5×10^3 [32] and Optimization
σ_l	3.5	[32] and Optimization	i_{0c}	8×10^{-2} [32] and Optimization
κ_{gdl}	1.18×10^{-11}	[32]	$\alpha_{a,a}$	0.5 [26] and Optimization
κ_{cl}	2.36×10^{-12}	[32]	$\alpha_{a,c}$	0.5 [26] and Optimization
ε_{gdl}	0.4	[32]	$\alpha_{c,a}$	0.53 [26] and Optimization
ε_{cl}	0.3	[32]	$\alpha_{c,c}$	0.47 [26] and Optimization
μ_a	1.19×10^{-5}	[28]	τ	1.4 [32]
μ_a	2.46×10^{-5}	[28]	T	318 Measured data

Table 1 shows the parameters used in the model, and Figure 4 shows the comparison between the experimental data and simulation results, where curve 1 represents that the cathode oxygen concentration is the same as that in air, and curve 2 represents that the cathode oxygen concentration is the same as the cathode outlet oxygen concentration at the minimum air mass flow rate of the fuel cell.

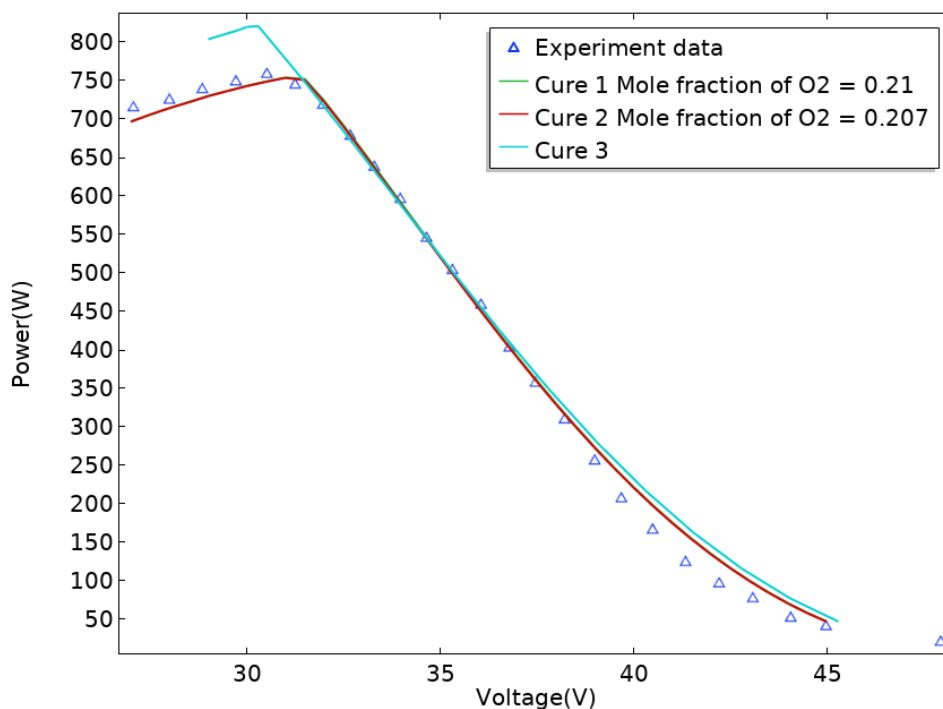


Figure 4. Comparison of the simulation results and experiment

Notably, curves 1 and 2 in the graph basically overlap, so it is certain that the variation in oxygen concentration under the condition of a sufficiently high air excess coefficient has little effect on the simulation results and can be neglected, and the previous assumptions about the simplification of the model geometry region in this paper are reasonable. Additionally, the experimental data and the simulation data can be in good agreement, so it can be considered that the model is applicable in this paper.

In this paper, a reference model was established with reference to the current modeling method for anode gas transport of PEMFCs fueled by pure hydrogen [25,26], and the simulation results obtained under the same characteristic parameters are shown by curve 3 in figure 4. It can be seen from the figure that in the right part of the curve, the difference between the simulation results is small, but when the voltage will reach the peak of the experimental data, the simulation results represented by curve 3 are higher than the experimental values, and this is exactly the stage when the concentration fraction of hydrogen in the fuel is greatly reduced due to continuous consumption. The model developed in this paper considers the effect of nitrogen on hydrogen concentration and diffusion. Figure 5 shows the molar concentration of hydrogen in the anode reaction layer obtained from the simulation model (a) and the reference model (b) at an output voltage of 0.6 V. Since the output power of the reference model is higher, the hydrogen concentration must be smaller in general than that of the simulation model in this paper, but it can be seen from the figure that the hydrogen concentration of the reference model is significantly higher than that of the simulation model in the rear section of the anode channel. This proves that the effect of nitrogen on the hydrogen substance transport must be considered under the condition of high concentration of nitrogen.

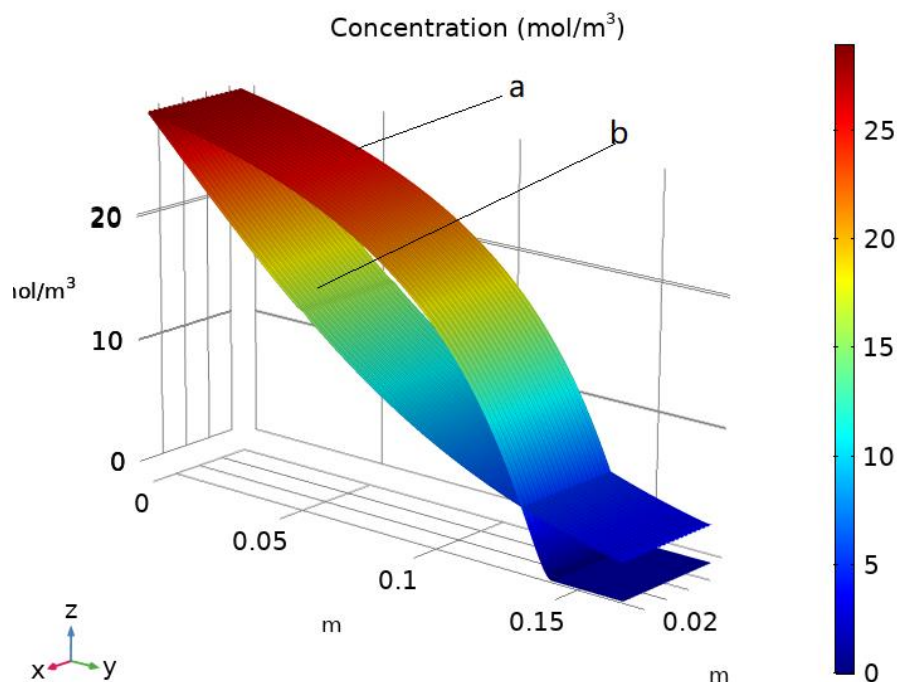


Figure 5. Molar concentration distribution of hydrogen within the anode reaction layer for different models when the voltage is equal to 0.6V

3.3 Local current density distribution of the PEM at different output voltages

Figure 6 shows the local current density distribution at different voltages. The local current density increases with decreasing output voltage at the anode inlet, but the opposite is true at the anode outlet. When the output voltage is too low, for example, $V=0.54$ in the figure, the local current density at the anode outlet drops sharply to zero, and the area with zero local current density near the anode outlet gradually expands as the output voltage decreases. The reason for the zero local current density when the output voltage is low is that the hydrogen concentration is close to zero due to the high consumption of hydrogen in the fuel. A low local current density can lead to a local overpotential in the PEM, which in turn can lead to deterioration of the PEM performance and therefore needs to be prevented. In Figure 6, it can also be seen that there are regular waves in the local current distribution surface, and the reason for this phenomenon is that the cathode runners and ribs lead to periodic changes in the cathode oxygen concentration, as shown in Figure 7. Moreover, there is a significant decrease at the anode entrance, which is also because the entrance corresponds exactly to the rib and wall, where the oxygen concentration is much lower. Figure 8 shows the local current density distribution along the anode for pure hydrogen and mixed gas at different output voltages, from which it can be seen that the local current density of pure hydrogen is always higher than that of mixed gas at the same output voltage. In particular, the closer to the anode channel exit, the larger the difference between the two cases. The lower the output voltage at the same position, the larger the difference between the two cases.

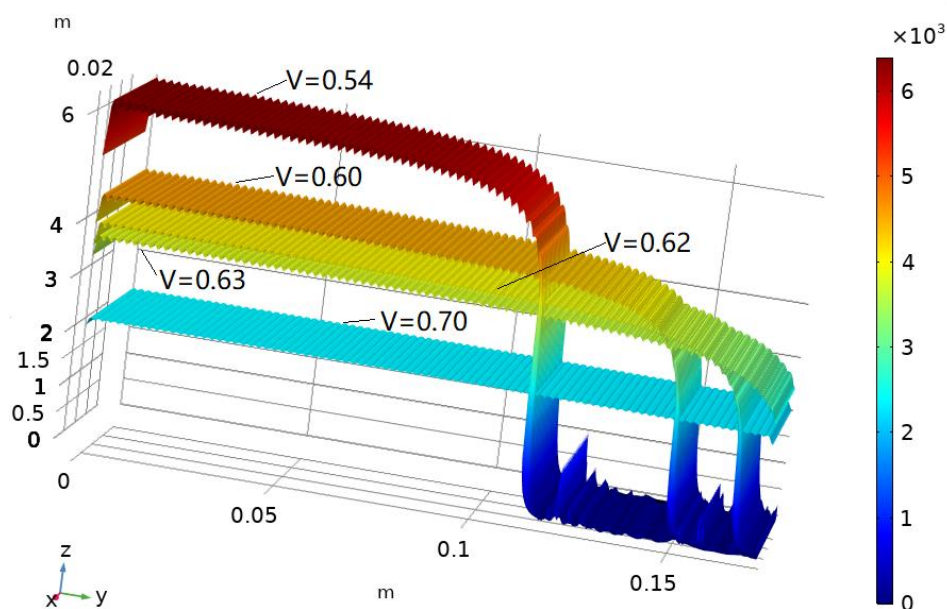


Figure 6. Local current density at different output voltages (the x-axis represents the cathode direction and the y-axis represents the anode direction)

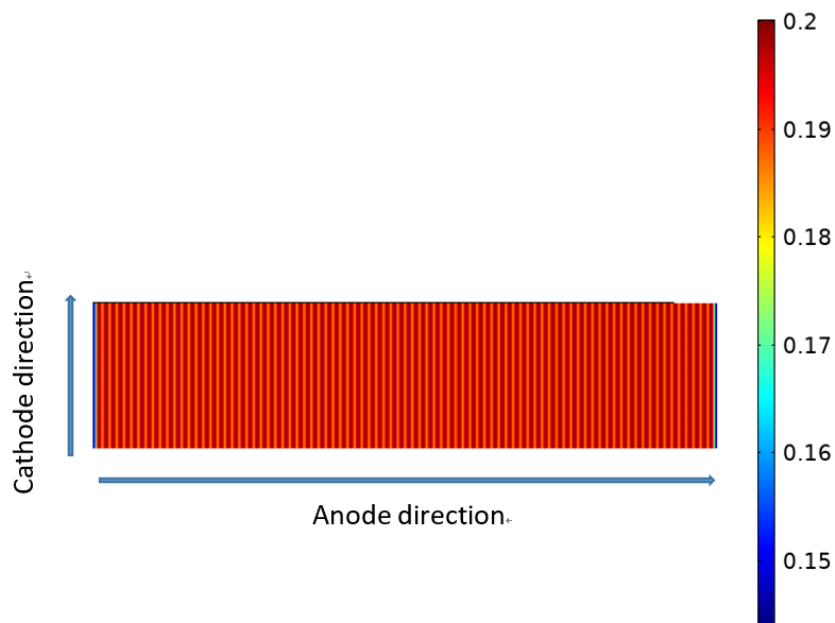


Figure 7. Local oxygen concentration distribution in the cathode catalyst layer

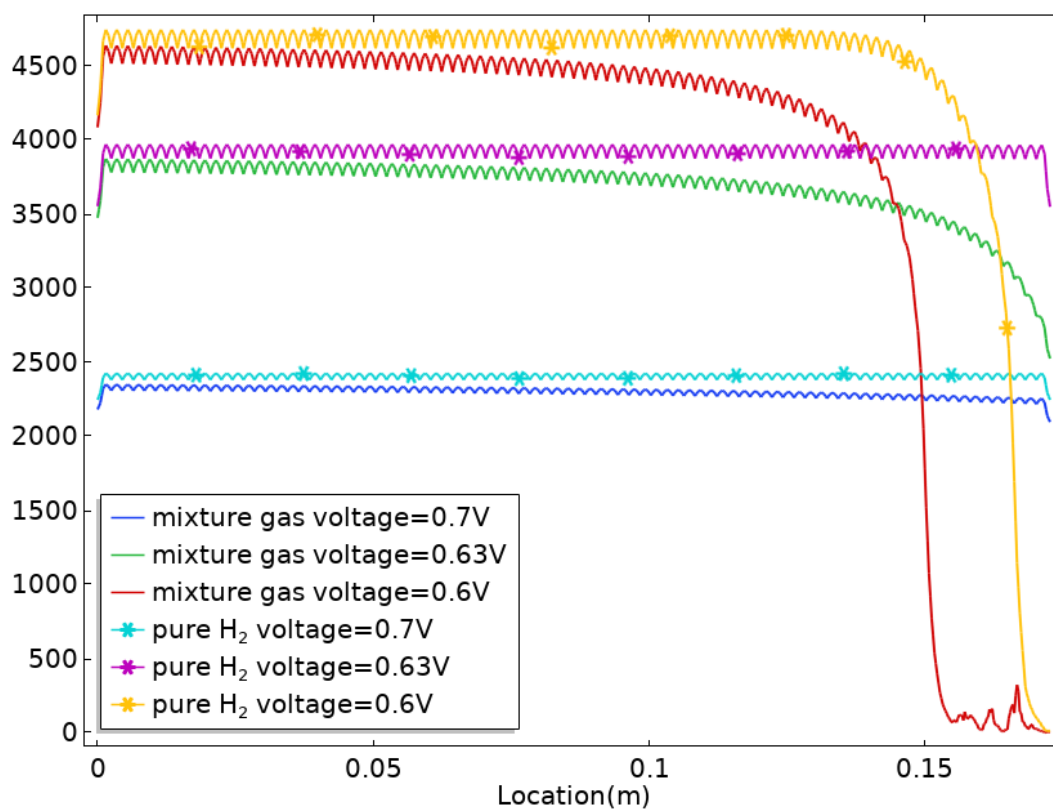


Figure 8. Local current density comparison chart

3.4 Distribution of the hydrogen concentration at different output voltages

Figure 9 shows the local concentration distribution of hydrogen in the anode catalyst layer at different output voltages. In the figure, when $V=0.54$, the molar concentration of hydrogen is close to 0 in the region near the anode exit, which also corresponds to the distribution of the zero local current density in Section 3.2. The hydrogen concentration distribution clearly varies along the anode runner until it drops to zero. However, the local current density distribution in Figure 6 shows an approximately uniform local current density distribution near the anode inlet. This result indicates that at higher hydrogen concentrations, the change in hydrogen concentration has little effect on the local current density, and the threshold value of the molar concentration is approximately 0.03 based on the simulation data. Additionally, a regular wave distribution appears in the direction along the cathode channel, which is caused by the influence of the anode ribs.

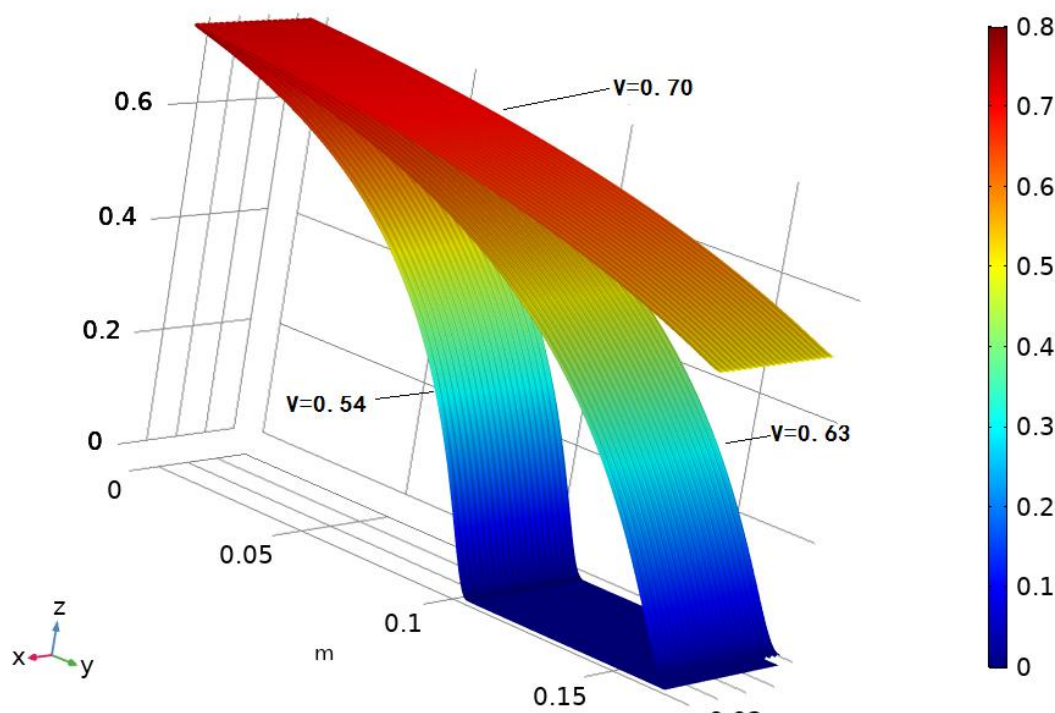


Figure 9. Local concentration distribution of hydrogen in the anode catalyst layer at different output voltages

Figure 10a shows the 3D distribution of the local molar concentration of hydrogen when the output voltage is $V=0.60$; notably, the molar concentration of hydrogen is significantly lower toward the end of the anode channel compared to the inlet. Figure 10b shows the local hydrogen molar distribution in the cross-section at different locations along the anode direction, and the figure shows a uniform concentration distribution. The above phenomena show that of the two effects of nitrogen on hydrogen, namely, the hydrogen concentration effect and diffusion effect, the former has a more influential effect on the output characteristics of the fuel cell.

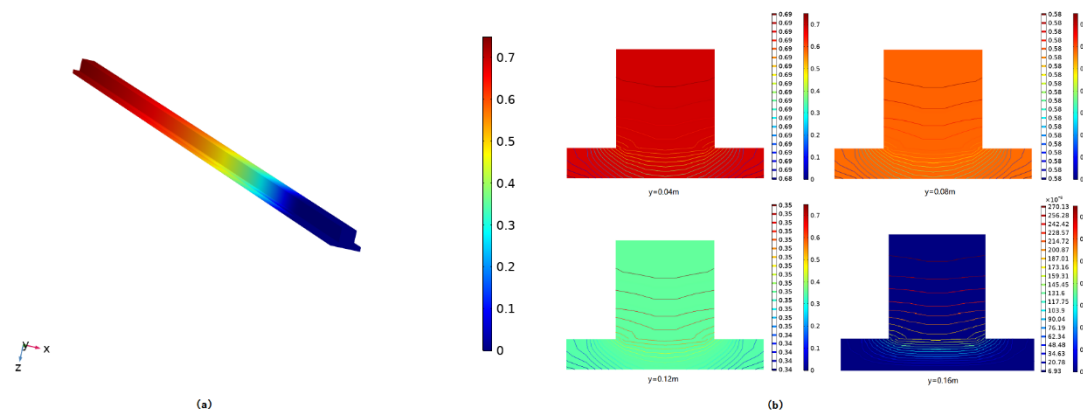


Figure 10. (a) 3D distribution of the local molar concentration of hydrogen and (b) distribution of the molar concentration of hydrogen in the cross-section at different positions along the anode direction

3.5 Output voltage and fuel utilization corresponding to the maximum efficiency of the fuel cell at different fuel flow rates

Figure 11 shows the maximum efficiency of the fuel cell at different fuel flow rates, as well as the output voltage and fuel utilization corresponding to the maximum efficiency. It can be seen from the figure that as the fuel flow rate decreases, the efficiency of the fuel cell increases, the fuel utilization remains basically the same (ranging from 0.891 to 0.889), and the output voltage gradually increases.

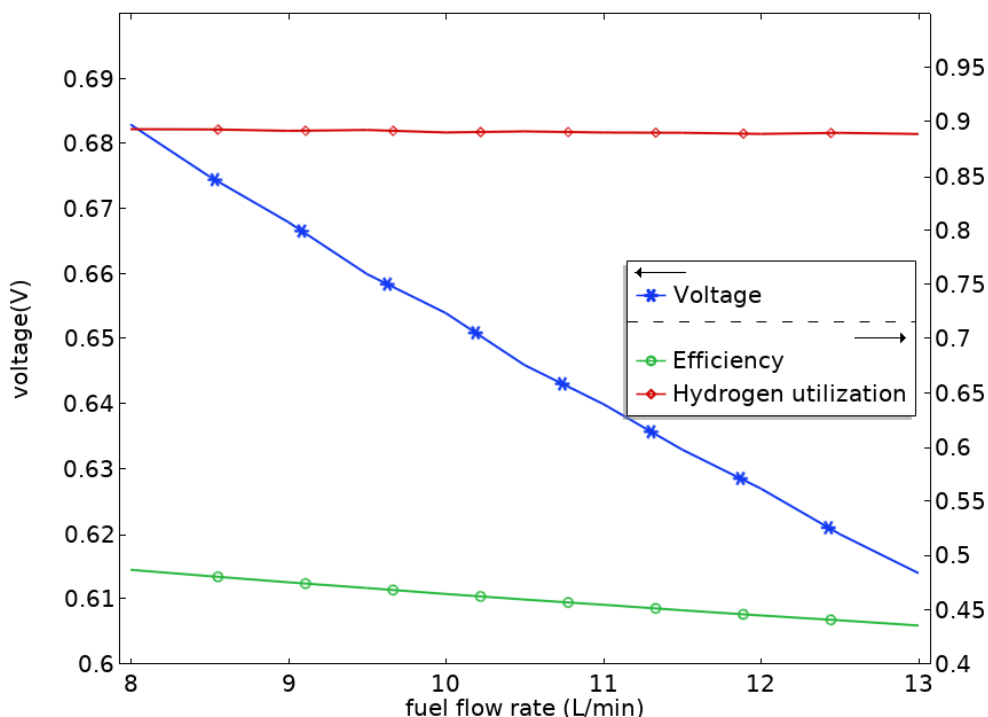


Figure 11. Maximum fuel cell efficiency at different fuel flow rates and corresponding output voltage and fuel utilization

3.6 Effect of the anode length on the max output power of the fuel cell

The above analysis shows that the presence of nitrogen causes an increase in the concentration difference polarization of the PEMFC, and this loss becomes more severe the closer the position is to the anode outlet. Therefore, the length of the anode will definitely have an effect on the output characteristics of the PEMFC. Therefore, in this paper, we study the output characteristics of the PEMFC with different anode lengths and the same plate area. Figure 12 shows the maximum power of the cell with different anode lengths and the corresponding voltage variation curve at a fuel flow rate of 12 L/min. It can be seen from the figure that the maximum output power increases as the anode length decreases, and the variation is basically linear. The maximum output power of the fuel cell increases by 7.75 W for every 10 mm decrease in anode length, which indicates that when designing a PEMFC that directly uses ammonia decomposition gas, the optimization aspect should be to minimize the length of the anode.

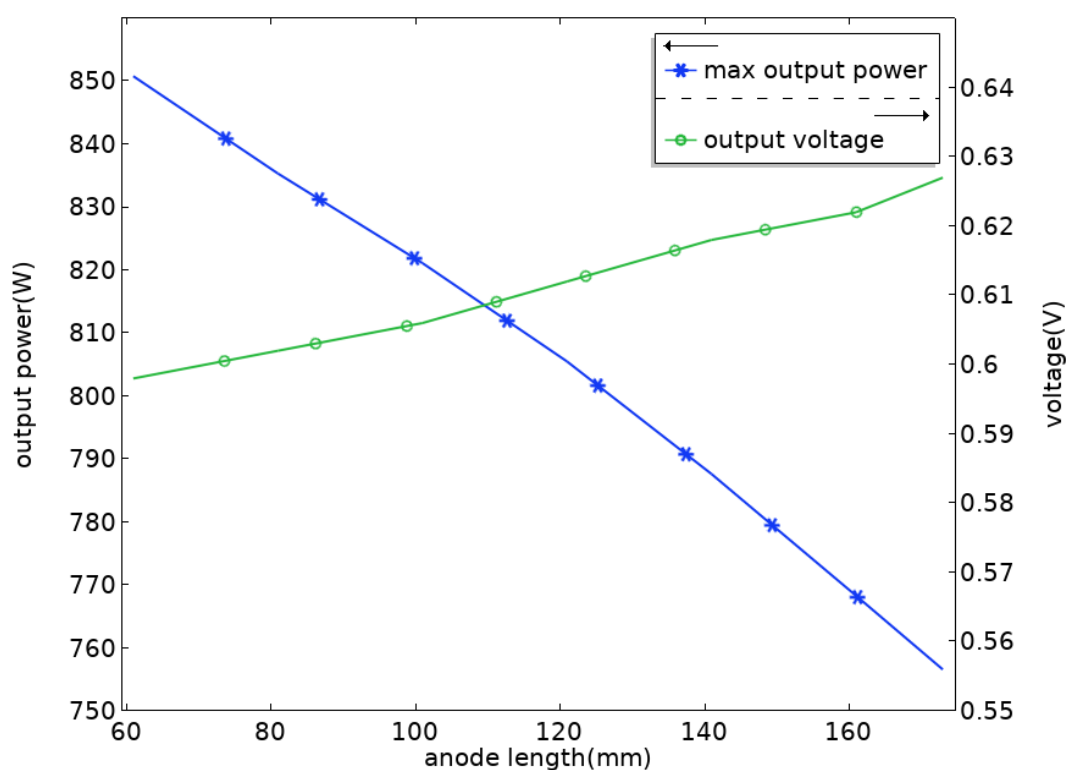


Figure 12. Maximum power and corresponding voltage variation curve of the fuel cell with different anode lengths

4. CONCLUSION

In this paper, a 3D simulation model of a PEMFC fueled by ammonia reforming gas is established, and the simulation model is modified by experimental data. The distribution of the local current density and local hydrogen concentration at different output voltages are studied and analyzed, and the threshold value of the local molar concentration of hydrogen affecting the local current density

is 0.03. The trend of the optimal efficiency of a fuel cell at different flow rates was studied, and the utilization rate of fuel at the optimal efficiency is approximately 0.89. Finally, a preliminary simulation analysis of the effect of the anode runner length on the maximum output power of the fuel cell is conducted, and it is found that the maximum output power of the fuel cell can be increased by reducing the anode runner length while keeping the same plate area. For every 10 mm decrease in anode length, the maximum output power of the fuel cell increases by 7.75 W. Therefore, a possible direction for the geometric optimization of a PEMFC anode for the direct use of ammonia decomposition gas as fuel is to minimize the length of the anode. The study results show that the PEMFC fueled by ammonia reforming gas can achieve good output characteristics with a reasonable flow control strategy and structural optimization, which indicates its potential for further research and development.

ACKNOWLEDGMENTS

The authors wish to thank the reviewers for their careful, unbiased, and constructive suggestions.

CONFLICTS OF INTEREST

“The authors declare that there are no conflicts of interest regarding the publication of this article.”

References

1. Energy & Climate Intelligence Unit. Net zero emissions race [EB/OL].<https://zerotracker.net/>(accessed on 20 June 2021).
2. L.Q. Fan, T. Cong, X.Y. Su, Q.J. Hu, Y.W. Wang, X.T. Liu, Y.F. Li, H.G. Jia and Y.P. Xiong, *Int. J. Electrochem. Sci.*, 15 (2020) 2839.
3. T.Y. Amiri, K. Ghasemzageh and A. Iulianelli, *Chem. Eng. Process.*, 157 (2020) 1.
4. S. Sengodan, L. Rong, J. Humphreys, D. Du and S. Tao, *Renewable Sustainable Energy Rev.*, 82 (2018) 761.
5. N. Lu and D. Xie, *Int. J. Chem. React. Eng.*, 14(1) (2016) 1.
6. A. Züttel, E. Callini, S. Kato and Z.Ö.K. Atakli, *Chimia*, 69(12) (2015) 741.
7. K. Fujita, T. Wada and T. Shiraishi, *Angew. Chem. Int. Ed.*, 56(36) (2017) 10886.
8. K.T. Møller, T.R. Jensen, E. Akiba and H.W. Li, *Prog. Nat. Sci.: Mater. Int.*, 27 (2017) 34.
9. P. Nikolaidis and A. Poullikkas, *Renewable Sustainable Energy Rev.*, 67 (2017) 597.
10. B. Sakintuna, F. Lamari-Darkrim and M. Hirscher, *Int. J. Hydrog. Energy*, 32 (2007) 1121.
11. A. Valera-Medina, H. Xiao, M. Owen-Jones, W.I.F. David and P.J. Bowen, *Prog. Energy Combust. Sci.*, 69 (2018) 63.
12. I. Garagounis, A. Vourros, D. Stoukides, D. Dasopoulos and M. Stoukides, *Membranes*, 9 (2019) 112.
13. Z.P. Cano, D. Banham, S. Ye, A. Hintennach, J. Lu, M. Fowler and Z. Chen, *Nat. Energy*, 3(4) (2018) 279.
14. V. Badescu, *Int. J. Energy Res.*, 44 (2020) 5360.
15. RenCat. Rencat technology[EB/OL].<https://rencat.net/Technology/> (accessed on 24 November 2021).
16. P. Sajjan, V. Nayak, M. Padaki, V.Y. Zadorozhnyy, S.N. Klyamkin and P. Konik, *Energy Fuels*, 34 (2020) 11699.
17. P. Hao, Y. Shi and N. Cai, *Int. J. Hydrogen Energy*, 46(1) (2021) 697.
18. Kamakshi, R. Kumar, V.K. Saraswat, M. Kumar and K. Awasthi, *Int. J. Hydrogen Energy*, 45(37)

- (2020) 18676.
19. H.M.A. Hunter, J.W. Makepeace, T.J. Wood, O.S. Mylius, M.G. Kibble, J.B. Nutter, M.O. Jones and W.I.F. David, *J. Power Sources*, 329 (2016) 138.
 20. A. Aiyejina and M. Sastry, *J. Electrochem. Energy Convers. Storage*, 9(1) (2012) 011011.
 21. Y. Chen, Z.G. Wan, X. Chen, X.Z. Kong, J. Zhang, T.M. Huang and X.D. Wang, *Energy Convers. Manage.*, 228(9) (2020) 113651.
 22. W.H. Chen, Z.L. Tsai, M.H. Chang, S.M. You and P.C. Kuo, *Int. J. Hydrogen Energy*, 46(31) (2021) 16717.
 23. O. Beruski, T. Lopes, A.R.J. Kucernak and J. Perez, *Phys.rev.fluids*, 2(10) (2017) 103501.
 24. Gwak and J. Lee J, *Int. J. Hydrogen Energy*, 45(24) (2020) 13414.
 25. S.H. Liu, T. Chen and Y. Xie, *Int. J. Green Energy*, 17(4) (2020) 255.
 26. N. Ahmadi, A. Dadvand, I. Mirzaei and S. Rezazadeh, *Int. J. Energy Res.*, 42(8) (2018) 2805.
 27. J.X. Liu, H. Guo, F. Ye and C.F. Ma, *ENERGY*, 119 (2017) 299.
 28. S.W. Tsai and Y.S. Chen, *Appl. Energy*, 188 (2017) 151.
 29. B.W. Wang, K.C. Wu, Z.R. Yang and K. Jiao, *Energy Convers. Manage.*, 171 (2018) 1463.
 30. J.F. Zhao, Q.C. Liang, Y.F. Liang, M.J. Li and J.Y. Hu, *J. Electrochem. Sci. Technol.*, (2021) In Press.
 31. E.T. Hashim and H.N.A. Al-Shorachi, *Pet. Sci. Technol.*, 25(8) (2007) 983.
 32. E.U. Ubong, Z. Shi and X. Wang, *J. Electrochem. Soc.*, 156(10) (2009) B1276.

© 2022 The Authors. Published by ESG (www.electrochemsci.org). This article is an open access article distributed under the terms and conditions of the Creative Commons Attribution license (<http://creativecommons.org/licenses/by/4.0/>).